ELSEVIER

Combustion and Flame 134 (2003) 35–53

Combustion and Flame

CSP analysis of a transient flame-vortex interaction: time scales and manifolds

Mauro Valorani[a], Habib N. Najm[b,*], Dimitris A. Goussis[c]

[a]*Dipartimento di Meccanica e Aeronautica, Via Eudossiana 18, 00184 Rome, Italy*
[b]*Sandia National Labs, 7011 East Ave, MS9051, Livermore, CA 94550, USA*
[c]*Agiou Georgiou 49, 26500 Rio, Greece*

Received 11 July 2002; received in revised form 26 February 2003; accepted 26 February 2003

Abstract

The interaction of a two-dimensional counter-rotating vortex-pair with a premixed methane-air flame is analyzed with the Computational Singular Perturbation (CSP) method. It is shown that, as the fastest chemical time scales become exhausted, the solution is attracted towards a manifold, whose dimension decreases as the number of exhausted time scales increases. A necessary condition for a chemical time scale to become exhausted is that it must be much faster than the locally prevailing diffusion and convection time scales. Downstream of the flame, the hot products are in a regime of near-equilibrium, characterized by a large number of exhausted fast chemical time scales and the development of a low dimensional manifold, where the dynamics are locally controlled by slow transport processes and slow kinetics. In the flame region, where intense chemical and transport activity takes place, the number of exhausted chemical time scales is relatively small. The manifold has a large dimension and the driving time scale is set by chemical kinetics. In the cold flow region, where mostly reactants are present, the flow regime can be described as frozen, as the active chemical time scales are much slower than the diffusion and convection time scales; the driving scale set by diffusion. The algebraic relations among the elementary rates, which describe the manifold, are discussed along with a classification of the unknowns in three classes: i) CSP radicals; ii) trace; and, iii) major species. It is established that the optimal CSP radicals must be: i) strongly affected by the exhausted fast chemical time scales; and, ii) significant participants in the algebraic relations describing the manifold. The identification of CSP radicals, trace and major species, is a prerequisite for simplification or reduction of chemical kinetic mechanisms.

Keywords: Flame; Vortex; CSP; Manifold; Equilibrium

1. Introduction

Computations of reacting flow with detailed chemical kinetics are necessary for developing fundamental understanding of the flow structure interaction with flames in turbulent combustion. Even for laminar flames, such computations are extremely challenging due to severe stiffness in the species conservation equations, caused by the large range of time and length scales encountered. The stiffness is created by a number of very fast chemical time scales, which are quickly exhausted, forcing the solution to evolve with the relatively slower scales on a manifold: a low dimensional surface in the phase space described by linearly independent relations among the elementary reaction rates [1,2]. This situ-

* Corresponding author. Tel.: +925-294-2054; fax: +925-294-2595.
E-mail address: hnnajm@ca.sandia.gov (H.N. Najm).

0010-2180/03/$ – see front matter
doi:10.1016/S0010-2180(03)00067-1

ation, involving the coexistence of fast and slow (locally exhausted and active, respectively) time scales, introduces severe difficulties in numerical time integration and spatial discretization.

The most accepted approach to resolve the stiffness problem is the simplification of the detailed chemical kinetic mechanism by suitable assumptions, which effectively removes the stiffness from the governing equations. Such simplifications are usually based on the partial-equilibrium and/or the steady-state approximations. The partial-equilibrium approximation [3] requires the identification of a number of fast elementary reactions that are in equilibrium either among themselves or with other slow elementary reactions. The construction of a simplified non-stiff kinetic mechanism on the basis of this kind of algebraic constraints is not common, since the simplification is possible only when the stoichiometric vectors of the reactions participating in the equilibrium assumption satisfy specific relations [4]. The steady-state approximation [5] requires the identification of species whose production and consumption rates are effectively balanced, so that their net production rates may be assumed to be zero. The resulting algebraic constraints on species concentrations always lead to a simplified non-stiff kinetic mechanism [4].

Lam and Goussis [4,6,7], and Hadjinicolaou and Goussis [8] discussed the advantages and disadvantages of these two techniques under different conditions. Clearly, one issue with both approaches is that the appropriate choice of steady-state species and fast reactions is difficult to make when dealing with large and complex kinetic mechanisms. Furthermore, the number and nature of steady-state and/or partial-equilibrium relations which develop depend on the local (in time and space) characteristics of the particular reacting flow under study. Thus, a species identified as steady-state at a particular point in space-time might be identified as a non steady-state species at a different point [9]. Similarly, an elementary reaction identified as fast/equilibrated at a particular point in space-time might be identified as a slow reaction, not participating in equilibrium relations, at a different point [9]. This situation makes the identification of steady-state species and fast equilibrated reactions a complicated subject. Furthermore, it was shown [4] that the conventional steady-state or partial-equilibrium assumptions do not provide the best accuracy possible; being a leading-order approximation to the optimal (in terms of accuracy) assumptions.

In the case of steady-state species in particular, a number of means of identifying them are found in the literature. In the past, such species were first defined as those whose production and destruction rate difference was much smaller than their sum. Other identification methods involved the magnitude of the candidate species properly scaled concentration [10], sensitivity analysis tools [11,12] and measures of species lifetime [13]. However, as we will discuss next in more detail, these methodologies are based on only a portion of the underlying physics.

A more complete picture can be obtained if the analysis of the system dynamics is based on: 1) the study of the chemical time scales and the directions in phase space along which they act; 2) the identification of those scales which are exhausted; and 3) the formulation of the algebraic relations describing the manifold on which the solution is constrained to evolve. As is by now well established, the number of algebraic relationships equals the number of the fast chemical time scales deemed exhausted. As a new fast chemical time scale becomes exhausted, the trajectory loses one more degree of freedom, i.e., it has no component in the direction along which the new exhausted time scale acts, and the dimension of the manifold decreases by one. This constraint is expressed as the emergence of an additional relation among the elementary reaction rates. The species most affected by such a constraint are those whose axis is the most parallel to the direction along which the time scale acts. Therefore, when a fast time scale becomes exhausted, the concentration of that species will, in essence, not change along this direction; i.e., it has achieved a "directional steady-state" status. The terminology used in the CSP literature refers to these species not as "steady-state" species but as "CSP radicals", to make clear the directional influence. The latter name is preferable, and will also be used in the present work. Such an approach in the identification of "steady-state species" was a significant by-product of the Computational Singular Perturbation (CSP) method [1,7,9,14].

It is reasonable to expect that the optimal selection for a CSP radical is a species which: 1) is among the most affected by the fast exhausted scales and, at the same time, 2) is among the most significant participants in the algebraic relations describing the manifold. Thus, when the existence of a manifold is utilized to arrive at a reduced chemical mechanism, CSP radicals are the optimal choice for species whose concentrations can directly be determined from the algebraic relationships defining the manifold.

In the present work, we both develop new extensions of CSP theory and use the CSP methodology to analyze coupled flame-flow dynamics in a multidimensional reacting flow involving the interaction of a two-dimensional counter-rotating vortex-pair with a premixed methane-air flame [15,16]. Such a flame configuration provides an excellent ground to test the

chemical-transport interaction. The methane-air system is relevant to general hydrocarbon combustion processes, yet is simple enough to allow large-scale numerical simulations with detailed kinetics. Moreover, this particular flame-vortex interaction has been studied extensively both numerically and experimentally, and is therefore of some general interest. One of the key questions pertains to the utility of reduced chemical mechanisms in modeling the transient coupled chemistry-transport processes inherent in this system. The present computations employ a detailed C_1C_2 chemical mechanism: GRImech1.2 involving 32 species, 4 elements and 177 reactions [17]. We first outline the theoretical formulation of the CSP method including the definitions of fast and slow modes with the associated manifold, and we extend this formulation to the realm of partial differential equations (PDEs) including convection and diffusion terms (section 2). Next, we present new CSP tools aimed at: 1) defining proper characteristic flow time scales (for diffusion, convection and chemistry) (section 3), and; 2) revising the concept of CSP radical, formerly introduced in [1,7] and its relation to time scales, algebraic constraints, and steady-state behavior (section 4). Finally, we define the reacting flow problem (section 5) and we analyze the transient vortex/flame interaction by means of the CSP tools to identify the number of exhausted chemical time scales at each point in space and time and their relation to the locally prevailing transport time scales (section 6). This information is used to gain physical understanding of the physical processes involved in the flame-flow interaction and to identify suitable exhausted modes and CSP radicals that can be used for the construction of a simplified locally-acceptable kinetics mechanism, with known error thresholds.

The computed time-evolving distributions of exhausted time scales and CSP radicals over the computational domain provide the basis for a rational adaptive chemistry approach in unsteady multidimensional reacting flow; whereby different regions of space can use different chemical mechanisms, as dictated by prespecified error thresholds.

2. CSP Basics

In the present work the diagnostic capabilities of CSP are extended to the realm of PDEs [8,10], to analyze computed reacting flow databases and acquire detailed physical understanding of flame/flow behavior.

The success of the CSP method in the analysis of reacting flow is based on the emergence of extremely fast time scales due to some components of the chemistry that act along specific directions in the space of the unknowns. If, along these "fast" directions, the influence of the other physical processes present - such as convection and diffusion - is sufficiently weak, the solution is forced to evolve on a manifold (a low dimensional surface in the space of the unknowns perpendicular to the "fast" directions) [8]. This manifold is described by linearly independent algebraic relations among the rates of some of the elementary reactions, the participation of the spatial operators (convection or diffusion) being of higher order [8]. These algebraic expressions describe the equilibration of the particular elementary reactions participating in the relations, which results in the constraints imposed on the evolution of the solution; i.e., its movement on the manifold. Of course, this condition does not hold when the transport time scales are equally fast or faster than the fastest chemical time scales; as in boundary layers.

CSP can identify the fast time scales due to chemistry, the specific "fast" directions in the space of the unknowns along which they act, and the shape of the manifold. As a result, it is straightforward to identify the reactions that are responsible for the emergence of these fast time scales, and the reactions whose rates are major participants in the relations describing the manifold. The identification of these reactions is very important, since the solution exhibits a fast adjustment to perturbations in their rates; the adjustment being more pronounced in the "fast" components of the solution (chemical species); i.e., the ones most affected by the fast chemical time scales [18]. In addition, CSP can identify the physical processes associated with the slow time scales in the problem (due to convection, diffusion and the slow part of chemistry), which determine the specific solution path on the manifold. Evidently, the adjustment of the solution to perturbations in the processes associated with the slow time scales is relatively slow [18].

It is assumed that the detailed kinetic mechanism consists of N_s species, E elements and N_r elementary reactions. Let us write the conservation equations of the N_s species mass fractions Y^i and the equation for the time rate of change of the temperature, T, in the CSP canonic form:

$$\frac{d\boldsymbol{y}}{dt} = \boldsymbol{L} + \boldsymbol{g} = \boldsymbol{L} + \boldsymbol{S}_1 R^1 + \boldsymbol{S}_2 R^2 + \ldots + \boldsymbol{S}_{2N_r} R^{2N_r} \quad (1)$$

where, $\boldsymbol{y}$ is the N-dimensional vector ($N = N_s + 1$) of the unknowns ($Y^1, \ldots, Y^{N_s}, T$), $\boldsymbol{L}$ represents the convective and diffusive spatial differential operators and $\boldsymbol{g}$ represents the chemical source term.

Further, the vectors $\boldsymbol{S}_1$ to $\boldsymbol{S}_{2Nr}$ define the (N,

$2N_r$)-dimensional generalized stoichiometric matrix S as

$$S = [\boldsymbol{S}_1, \boldsymbol{S}_2, \ldots, \boldsymbol{S}_{2N_r}] = [Q\boldsymbol{\mathcal{S}}, Q\boldsymbol{\mathcal{S}}] \tag{2}$$

where the (N_s, N_r) matrix of stoichiometric coefficients $\boldsymbol{\mathcal{S}}$ is defined as:

$$\boldsymbol{\mathcal{S}}_{ik} = \nu_{ik},\ i = 1, \ldots, N_s;\ k = 1, \ldots, N_r \tag{3}$$

where ν_{ik} is the net stoichiometric coefficient of species i in reaction k and the (N, N_s) matrix Q is defined as:

$$Q = \begin{bmatrix} \frac{DaW_1}{\rho} & 0 & \ldots & 0 & 0 \\ 0 & \frac{DaW_2}{\rho} & \ldots & 0 & 0 \\ \ldots & 0 & \ldots & \ldots & \ldots \\ 0 & \ldots & \ldots & 0 & \frac{DaW_{N_s}}{\rho} \\ -\frac{DaW_1}{\rho c_p} h_1 & \ldots & \ldots & -\frac{DaW_1}{\rho c_p} h_{N_s-1} & -\frac{DaW_1}{\rho c_p} h_{N_s} \end{bmatrix}.$$

where ρ is the mixture density, W_i is molecular weight of the i-th species, Da is the Damköhler number, and c_p is the average specific heat at constant pressure of the mixture.

Finally, the rates R^1 to R^{2N_r} define the generalized $(2\ N_r)$-dimensional vector $\boldsymbol{R}$ as:

$$\boldsymbol{R} = [r_{f,1}, r_{f,2}, \ldots, r_{f,N_r}, -r_{b,1}, -r_{b,2}, \ldots, -r_{b,N_r}] \tag{4}$$

where r_f and r_b are the third-body and pressure-fall-off corrected (if applicable) forward and reverse rates of progress of the N_r reversible reactions.

Introducing the CSP basis vectors $\boldsymbol{a}_i$ and $\boldsymbol{b}^i$ $(i = 1, N)$, first proposed in [1,7,8], which satisfy the relations $\boldsymbol{b}^i \cdot \boldsymbol{a}_m = \delta^i_m$ and $\sum_{i=1,N} \boldsymbol{a}_i \boldsymbol{b}^i = I$, allows us to cast Eq. (1) as:

$$\frac{d\boldsymbol{y}}{dt} = \sum_{i=1,N} \boldsymbol{a}_i h^i \tag{5}$$

where the modal amplitudes h^i are defined as:

$$h^i = \boldsymbol{b}^i \cdot \boldsymbol{L} + (\boldsymbol{b}^i \cdot \boldsymbol{S}_1) R^1 + (\boldsymbol{b}^i \cdot \boldsymbol{S}_2) R^2 + \ldots + (\boldsymbol{b}^i \cdot \boldsymbol{S}_{2N_r}) R^{2N_r} \tag{6}$$

Note that the CSP basis vectors are determined on the basis of the chemical source term only. The N CSP-modes in Eq. (5) are ordered so that the first $(i = 1)$ mode refers to the fastest chemical time scale, the second $(i = 2)$ mode refers to the second fastest, etc. When the amplitudes of the M fastest modes have vanished, i.e. when the the following relations hold:

$$h^r \approx 0 \qquad r = 1, M \tag{7}$$

then we will declare "exhausted" the chemical time scales τ^r_{chem} $(r = 1, M)$ and "fast" the corresponding modes. The remaining $N - M$ time scales and modes are declared as being "active" and "slow", respectively. Equations (7) express the equilibration of the different terms in the expression of each h^r, as in Eq. (6), the cancellations among the elementary rates being the most important [8].

It might also occur that the amplitude of any mode h^i is zero or very small not because of the action of the different participating processes balancing one another along the direction of the mode, but because each term in the expression h^i, as in Eq. (6), is either very small or zero. In this case, we will refer to the mode, either fast or slow, as a dormant mode [7]. Unlike exhausted fast modes, the dormant modes do not produce equations of state. However, like an exhausted fast mode, the presence of a dormant mode indicates a decrease by one of the dimensions of the subdomain in which the solution can evolve, by not allowing the spreading of the manifold along their directions.

Therefore, at each point in time and space, the role of the reactions and the other physical processes in the problem (convection and diffusion) which are responsible for the emergence of fast exhausted and/or dormant modes is in a sense passive, when viewed from the fast directions point of view. In particular they tend to diminish the domain in which the solution is allowed to move; the exhausted fast modes by restricting its trajectory on the manifold and the dormant fast modes by not allowing the manifold to spread along their directions, both by virtue of the constraints expressed in Eq. (7). On the other hand, the role of the processes responsible for the emergence of the non-exhausted, non-dormant modes is active; i.e., they determine the specific trajectory and speed on the manifold on which the

solution evolves according to the set of simplified (non-stiff) PDE's:

$$\frac{d\boldsymbol{y}}{dt} = \sum_{s=M+1,N} \boldsymbol{a}_s h^s \tag{8}$$

in which both slow active and slow dormant modes participate. Note here that a physical process, either reaction or transport, can participate simultaneously in the fast exhausted or dormant modes and the slow active or dormant ones. The criterion that determines the number of exhausted time scales M, is based on the definition of an error vector $\boldsymbol{y}_{error}$ built on the basis of the solution vector $\boldsymbol{y}$, as follows:

$$y^i_{error} = \epsilon^i_{rel}\, y^i + \epsilon^i_{abs} \qquad i = 1, N \tag{9}$$

where ϵ^i_{rel} and ϵ^i_{abs} are the maximum relative and absolute errors on the i-th element of the state vector $\boldsymbol{y}$, respectively. The number M of time scales which, within the limits of accuracy specified by the given error vector, are considered exhausted, is defined as the largest integer lying between 1 and N which satisfies the following inequality for each $i = 1, N$:

$$|\tau^{M+1}_{chem} \sum_{r=1}^{M} a^i_r h^r| < \boldsymbol{y}^i_{error} \tag{10}$$

where τ^{M+1}_{chem} is the fastest of the active chemical time scales.

The criterion adopted to identify if the m-th mode is dormant is:

$$\begin{aligned} &|\boldsymbol{b}^i \cdot \boldsymbol{L}| + |(\boldsymbol{b}^i \cdot \boldsymbol{S}_1) R^1| + |(\boldsymbol{b}^i \cdot \boldsymbol{S}_2) R^2| \\ &\qquad + \ldots\ldots + |(\boldsymbol{b}^i \cdot \boldsymbol{S}_{2N_r}) R^{2N_r}| \\ &< |\lambda^{M+1} \boldsymbol{b}^i \cdot \boldsymbol{y}_{err}| \end{aligned} \tag{11}$$

for each $i = 1, N$.

A dormant mode can originate when the chemistry is frozen with respect to convection and diffusion, i.e., when the characteristic chemical time scales are much slower than the characteristic time scales of convection and diffusion. Note that a dormant mode can relate to either the M exhausted time scales or the $N - M$ slow time scales.

A dormant mode can be safely dropped in the modal expansion of the right-hand-side of Eq. (5) without any loss in accuracy. This also implies that when a number N_d of dormant modes is present at a given space and time location, then the actual dimension of the system locally reduces to $N - N_d$ corresponding to the total number of degrees of freedom available to the system space vector in the phase space.

Some of the dormant modes will be found among the M exhausted time scales, say N^{fast}_d. In this case, the number of algebraic relations describing the manifold reduces to $M - N^{fast}_d$.

The number of active modes describing the slow dynamics of the system is therefore: $N - (N_d - N^{fast}_d) - M$. This number turns out to be the dimension of the manifold as well.

3. Time scales in reaction-diffusion-convective problems

As mentioned in the introduction, the fastest chemical time scales tend to prevent the system space vector from moving in the directions along which they act. The development of the manifold is a direct result of this behavior. However, diffusion or convection might develop equally fast time scales along these directions, preventing the manifold to develop. In the following, we will outline the rationale followed to define a set of characteristic time scales for both the spatial operators and the chemical source term.

Consider Eq. (1) where the spatial operator $\boldsymbol{L}$ is explicitly written as the sum of the diffusive and convective operators:

$$\frac{d\boldsymbol{y}}{dt} = \boldsymbol{L}_d(\boldsymbol{y}) + \boldsymbol{L}_c(\boldsymbol{y}) + \boldsymbol{g}(\boldsymbol{y}) \tag{12}$$

where $\boldsymbol{L}_d$ and $\boldsymbol{L}_c$ are the N-dimensional diffusive and convective differential operators for a (spatially) one-dimensional problem and $\boldsymbol{g}$ is an N-dimensional algebraic function:

$$\boldsymbol{L}_d(\boldsymbol{y}) = \begin{bmatrix} L^1_d(y^1, \ldots, y^N) \\ \vdots \\ L^N_d(y^1, \ldots, y^N) \end{bmatrix}$$

$$\boldsymbol{L}_c(\boldsymbol{y}) = \begin{bmatrix} L_c(y^1) \\ \vdots \\ L_c(y^N) \end{bmatrix}$$

$$\boldsymbol{g}(\boldsymbol{y}) = \begin{bmatrix} g^1(y^1, \ldots, y^N) \\ \vdots \\ g^N(y^1, \ldots, y^N) \end{bmatrix}$$

Consider two neighboring points on the solution trajectory: $\boldsymbol{y}_o$ $(t = t_o, \boldsymbol{x} = \boldsymbol{x}_o)$ and $\boldsymbol{y}(t = t_o + \Delta t, \boldsymbol{x} = \boldsymbol{x}_o + \Delta \boldsymbol{x})$. Let $\boldsymbol{\alpha}_i$ and $\boldsymbol{\beta}^i$ be the right (column) and left (row) constant eigenvectors of J_o, where $J_o = J(\boldsymbol{y}_o)$ is the Jacobian of $\boldsymbol{g}$ at $\boldsymbol{y} = \boldsymbol{y}_o$, $\boldsymbol{\beta}^i \cdot \boldsymbol{\alpha}_j = \delta^i_j$ and $\lambda(i)$ the related eigenvalue. Multiplying Eq. (12) with $\boldsymbol{\beta}^i$ yields:

$$\frac{d(\boldsymbol{\beta}^i \cdot \boldsymbol{y})}{dt} = \boldsymbol{\beta}^i \cdot \boldsymbol{L}_d(\boldsymbol{y}) + \boldsymbol{\beta}^i \cdot \boldsymbol{L}_c(\boldsymbol{y}) + f^i(\boldsymbol{y}) \tag{13}$$

for $i = 1, N$ and where $f^i(\boldsymbol{y}) = \boldsymbol{\beta}^i \cdot \boldsymbol{g}(\boldsymbol{y})$. Integrating Eq. (13) over a time step Δt yields to leading order:

$$\boldsymbol{\beta}^i \cdot \mathbf{y}_1 \approx \boldsymbol{\beta}^i \cdot \mathbf{y}_o + [\boldsymbol{\beta}^i \cdot \mathbf{L}_{d,o} + \boldsymbol{\beta}^i \cdot \mathbf{L}_{c,o} + f^i_o]\Delta t \tag{14}$$

where $\mathbf{L}_{d,o} = \mathbf{L}_d(\mathbf{y}_o)$, $\mathbf{L}_{c,o} = \mathbf{L}_c(\mathbf{y}_o)$ and $f^i_o = \boldsymbol{\beta}^i \cdot \mathbf{g}(\mathbf{y}_o)$. Assuming $\boldsymbol{\beta}^i \cdot \mathbf{y}_o$ to be nonzero, Eq. (14) yields:

$$\frac{\boldsymbol{\beta}^i \cdot \mathbf{y}_1}{\boldsymbol{\beta}^i \cdot \mathbf{y}_o} \approx 1 + \frac{\boldsymbol{\beta}^i \cdot \mathbf{L}_{d,o} + \boldsymbol{\beta}^i \cdot \mathbf{L}_{c,o} + f^i_o}{\boldsymbol{\beta}^i \cdot \mathbf{y}_o}\Delta t \tag{15}$$

or:

$$\begin{aligned}\mathbf{y}_1 \approx \mathbf{y}_0 &+ \sum_{i=1,N} \boldsymbol{\alpha}_i (e^{\frac{\boldsymbol{\beta}^i \cdot \mathbf{L}_{d,0}}{\boldsymbol{\beta}^i \cdot \mathbf{y}_0}\Delta t} - 1)(\boldsymbol{\beta}^i \cdot \mathbf{y}_0) \\ &+ \sum_{i=1,N} \boldsymbol{\alpha}_i (e^{\frac{\boldsymbol{\beta}^i \cdot \mathbf{L}_{c,0}}{\boldsymbol{\beta}^i \cdot \mathbf{y}_0}\Delta t} - 1)(\boldsymbol{\beta}^i \cdot \mathbf{y}_0) \\ &+ \sum_{i=1,N} \boldsymbol{\alpha}_i \frac{f^i_0}{\lambda(i)} (e^{\lambda(i)\Delta t} - 1)\end{aligned} \tag{16}$$

for integration time steps Δt which satisfy the relation:

$$\max(|(\boldsymbol{\beta}^i \cdot \mathbf{L}_{d,o}/\boldsymbol{\beta}^i \cdot \mathbf{y}_o)\Delta t|, |(\boldsymbol{\beta}^i \cdot \mathbf{L}_{c,o}/\boldsymbol{\beta}^i \cdot \mathbf{y}_o)\Delta t|, |\lambda(i)\Delta t|) \ll 1.$$

It follows that one can define diffusive, convective and chemical time scales for the i-th mode as:

$$\tau^i_{diff} = \left|\frac{\boldsymbol{\beta}^i \cdot \mathbf{y}_o}{\boldsymbol{\beta}^i \cdot \mathbf{L}_{d,o}}\right|$$

$$\tau^i_{conv} = \left|\frac{\boldsymbol{\beta}^i \cdot \mathbf{y}_o}{\boldsymbol{\beta}^i \cdot \mathbf{L}_{c,o}}\right|$$

$$\tau^i_{chem} = \left|\frac{1}{\lambda(i)}\right|$$

These are time scales related to the three physical processes in the problem acting along the direction $\mathbf{a}_i$. Since, according to Eq. (8), the solution moves along a trajectory in an $N - M$ subdomain defined by the basis vectors $\mathbf{a}_{M+1}$ to $\mathbf{a}_N$, the driving time scale, $\tau_{driving}$, locally controlling the flow evolution is given by:

$$\begin{aligned}\tau_{driving} = \min(&\tau^{M+1}_{chem}, \tau^{M+1}_{diff}, \ldots, \\ &\cdot \tau^N_{diff}, \tau^{M+1}_{conv}, \ldots, \tau^N_{conv})\end{aligned} \tag{18}$$

4. Classification of unknowns

Each unknown, say a species or the temperature, plays a different role during the system evolution. Some unknowns evolve with the fastest active time scales or react immediately to perturbations along the fast directions, while others evolve with slower scales or do not react to these perturbations. In addition, some unknowns participate in the algebraic relations which define the manifold geometry and others do not. It is therefore mandatory that the CSP analysis be able to identify the role of each unknown as the system evolves in time and space.

More specifically, one has to find an answer to these questions:

1. When is an unknown affected by a fast time scale?
2. When does an unknown participate in the algebraic relation describing the manifold?
3. Which unknown, typically a species, plays a negligible role in the system dynamics at a given spatial location and time so that it can be safely removed from the set of unknowns?

It will be shown that unknowns which are both; 1) strongly affected by the fast time scales; and, 2) significantly participate in the algebraic relationships describing the manifold, are the best candidates to be used as CSP radicals, i.e., as species whose concentrations can directly be computed from these algebraic relationships.

To carry out this analysis, we consider a system of N ODE's of the form:

$$\frac{d\mathbf{y}}{dt} = \mathbf{g}(\mathbf{y}) \tag{19}$$

where, for simplicity, the transport terms are neglected.

Perturbing Eq. (19) at $t = t_o$ yields the equations describing the evolution of the perturbations $\delta\mathbf{y} = \mathbf{y} - \mathbf{y}_o$ along the trajectory:

$$\frac{d\delta\mathbf{y}}{dt} = \mathbf{g}(\mathbf{y}_o) + J(\mathbf{y}_o)\delta\mathbf{y} \tag{20}$$

where $\mathbf{y}_o$ is a point on the trajectory and $J(\mathbf{y}_o)$ is the Jacobian of $\mathbf{g}$, both evaluated at $t = t_o$.

4.1. CSP radicals

Let $\boldsymbol{\alpha}_i$ and $\boldsymbol{\beta}^i$ be the right (column) and left (row) eigenvectors of $J(\mathbf{y}_o)$, and $\lambda(i)$ the related eigenvalue, where $i = 1, N$. Then, Eq. (20) can be cast as:

$$\begin{aligned}\frac{d\delta\mathbf{y}}{dt} &= \sum_{i=1,N} \boldsymbol{\alpha}_i \boldsymbol{\beta}^i [\mathbf{g}(\mathbf{y}_o) + J(\mathbf{y}_o)\delta\mathbf{y}] \\ &= \sum_{i=1,N} \boldsymbol{\alpha}_i [f^i(\mathbf{y}_o) + \lambda(i)\boldsymbol{\beta}^i \cdot \delta\mathbf{y}]\end{aligned} \tag{21}$$

where $f^i = \boldsymbol{\beta}^i \cdot \mathbf{g}$. Assuming that the M fastest modes are exhausted at $t = t_o + \Delta t$ yields the following set of N equations:

$$\sum_{r=1,M} \boldsymbol{\alpha}_r[f^r(\mathbf{y}_o) + \lambda(r)\boldsymbol{\beta}^r \cdot \delta\mathbf{y}] \approx 0 \tag{22}$$

These are N equations, only M of which are linearly independent. In fact, Eq. (22) is satisfied only if each term in the square brackets is zero, that is only if the following M linearly independent relations hold:

$$f^r(\mathbf{y}_o + \delta\mathbf{y}) = f^r(\mathbf{y}_o) + \lambda(r)\boldsymbol{\beta}^r \cdot \delta\mathbf{y} \approx 0 \qquad r = 1, M \tag{23}$$

This set of equations is under-determined, since there are N unknowns (the N-dimensional vector $\delta\mathbf{y}$, or the vector $\mathbf{y}$) and only M equations. Thus, the question is for which M unknowns to solve the M equations with the remaining $N - M$ unknowns treated as known parameters. These M unknowns will be named CSP radicals [19], and are identified according to the following procedure. By assuming that the M fastest modes are exhausted at $t = t_o$ as well as $t = t_o + \Delta t$, i.e., $f^i(\mathbf{y}_o) \approx 0$, we can write Eq. (22) as:

$$\sum_{r=1,M} \boldsymbol{\alpha}_r[\lambda(r)\boldsymbol{\beta}^r \cdot \delta\mathbf{y}] \approx 0 \tag{24}$$

or, since the basis vectors are linearly independent, as:

$$[\boldsymbol{\alpha}_r\boldsymbol{\beta}^r]\delta\mathbf{y} \approx 0 \tag{25}$$

for each $r = 1, M$. These M equations may be linearly combined into a single set according to the expression:

$$\begin{bmatrix} \Sigma_{i=1,M}\alpha_i^1\beta_1^i & \Sigma_{i=1,M}\alpha_i^1\beta_2^i & \cdots & \Sigma_{i=1,M}\alpha_i^1\beta_N^i \\ \Sigma_{i=1,M}\alpha_i^2\beta_1^i & \Sigma_{i=1,M}\alpha_i^2\beta_2^i & \cdots & \Sigma_{i=1,M}\alpha_i^2\beta_N^i \\ \vdots & \vdots & & \vdots \\ \Sigma_{i=1,M}\alpha_i^N\beta_1^i & \Sigma_{i=1,M}\alpha_i^N\beta_2^i & \cdots & \Sigma_{i=1,M}\alpha_i^N\beta_N^i \end{bmatrix} \begin{bmatrix} \delta y^1 \\ \delta y^2 \\ \vdots \\ \delta y^N \end{bmatrix} \approx 0 \tag{26}$$

Eq. (26) consists of N equations, of which only M are linearly independent. Each element $\Sigma_{i=1,M}\alpha_i^k\beta_k^i$ on the diagonal of the dyadic above is referred to as the CSP pointer to species k from the pool of M fast modes. The M largest (absolute) values among the diagonal elements of the dyadic $\Sigma_{i=1,M}\boldsymbol{\alpha}_i\boldsymbol{\beta}^i$ identify the non-singular ($M \times M$) minor of Eq. (26) with the largest condition number and the corresponding M unknowns δy^k, the CSP radicals, with respect to which Eq. (26), and Eq. (23) as well, can be accurately solved.

Now suppose that only one mode, say the j-th, contributes to order one to the summation $\Sigma_{i=1,M}\alpha_i^k\beta_k^i$, all others contributing to order ε, then it is possible to state that species y^k is *the* CSP radical associated with mode i. However, it might also occur that two (or more modes) contribute to order one to the summation. In this latter case, species y^k is still a CSP radical but cannot be associated with a single mode: among other consequences, this implies that species y^k is affected simultaneously by the time scales of both modes.

Now, let us look at the same problem from a different angle. By setting $\delta\mathbf{y} = \mathbf{y}_1 - \mathbf{y}_0$ in Eq. (16) and having set the transport terms to zero yields:

$$\delta\mathbf{y} = \sum_{i=1,N} \boldsymbol{\alpha}_i(e^{\lambda(i)\Delta t} - 1)\left(\frac{1}{\lambda(i)} f^i(\mathbf{y}_o)\right) \tag{27}$$

which shows that the time scale $\tau(i) = |1/\lambda(i)|$ acts along the direction $\boldsymbol{\alpha}_i$.

This action might be felt by the unknowns only when the i-th time scale is not exhausted, i.e., f^i is not zero. Once the solution reaches the manifold and moves along it, then f^i is nearly zero; thus, the action of the time scale $\tau(i)$ might be felt only if a perturbation is applied to the state vector along the $\boldsymbol{\alpha}_i$ direction, resulting in a non-zero f^i. This perturbation will subside in an order $\tau(i)$ time span.

Taking the product of the row vector $\boldsymbol{e}^k$ (defined as a row vector with all elements zero but for the k-th element which is set equal to 1) with the column vector solution of Eq. (27), and scaling both members of the equation by y_o^k, yields:

$$\frac{\boldsymbol{e}^k \cdot \delta\mathbf{y}}{y_o^k} = \frac{\delta y^k}{y_o^k} = \sum_{i=1,N} \frac{\boldsymbol{e}^k \cdot \boldsymbol{\alpha}_i}{y_o^k}(e^{\lambda(i)\Delta t} - 1) \cdot \left(\frac{1}{\lambda(i)} f^i(\mathbf{y}_o)\right) \tag{28}$$

Clearly if $\boldsymbol{e}^k \cdot \boldsymbol{\alpha}_i \neq 0$, then δy^k (or y^k) is in principle affected by $\lambda(i)$. Moreover, the larger the value of $|\boldsymbol{e}^k \cdot \boldsymbol{\alpha}_i / y_o^k|$, the larger is the effect of the i-th time scale on the k-th unknown.

Furthermore, since $f^i(\mathbf{y}_o) \approx 0$ in Eq. (23), we have:

$$\boldsymbol{\beta}^i \cdot \delta\mathbf{y} \approx 0$$

that is:

$$(\boldsymbol{\beta}^i \cdot \boldsymbol{e}_1 y_o^1)\left(\frac{y^1}{y_o^1} - 1\right) + (\boldsymbol{\beta}^i \cdot \boldsymbol{e}_2 y_o^2)\left(\frac{y^2}{y_o^2} - 1\right) + \ldots + (\boldsymbol{\beta}^i \cdot \boldsymbol{e}_N y_o^N)\left(\frac{y^N}{y_o^N} - 1\right) \approx 0 \tag{29}$$

where $\boldsymbol{e}_k$ is a column vector orthogonal to $\boldsymbol{e}^k$.

Clearly, the larger the value of $|\boldsymbol{\beta}^i \cdot \boldsymbol{e}_k \mathbf{y}_o^k|$, the more significant the participation of the k-th un-

known y^k in the cancellations occurring in the algebraic relation $f^i(\boldsymbol{y}_o + \delta\boldsymbol{y}) \approx 0$.

4.2. Trace species

The CSP pointer allows us to associate the exhausted modes with the CSP radicals; i.e., those having the largest pointer. However, the species thus selected belong to two different categories: true CSP radicals resulting from finite but fast/exhausted modes, and "trace" species. In fact, at a given time and space, some of the species might contribute to the mixture composition very little, either because they have not yet been produced from the reactants or because they have been entirely consumed. We are thus tempted to declare these species as "trace."

However, "being small" is a necessary condition to declare a species "trace," but not sufficient: radicals in the pre-heat flame zone, although initially present in small amount, are bound to grow at later times, and, therefore, cannot be considered trace as far as the flame dynamics is concerned.

A criterion to discriminate if a small species will or will not affect the flow dynamics at later times, might be based on the sign of the corresponding chemical source term: when this is negative, one can infer that the species present in small amount will remain as such on a time scale of the order of the integration time step. In this instance, the species can be safely labeled as "trace," since it is not contributing to the flow dynamics and mixture state.

This criterion was first introduced in [20] as a part of the CSP-based, explicit, time-scale split algorithm. To summarize, we declare that the i-th species is a "trace species" if:

$$|y_i| < y_{\text{tolerance}} \text{ and } g_i < 0 \tag{30}$$

where g_i includes the chemical source term alone, without convection and diffusion.

Therefore, the only species legitimately definable as being CSP radicals are those which are simultaneously associated with the exhausted modes via the CSP pointer and are not "trace species."

Note that the number of trace species can be larger than the number of exhausted modes. In this case, not all the species associated by the CSP pointers with the exhausted modes need to be trace.

Also note that a trace species is often associated with a dormant mode. This circumstance can provide significant savings of computational work when a reduced mechanism is adopted instead of the complete one, since the total work to solve the nonlinear algebraic system describing the manifold is proportional to $(M - N_d^{fast})^2$, once the N_d^{fast} trace species and the corresponding dormant modes are removed from the set of unknowns and the modal expansion of the right-hand side of Eq. (5), respectively.

4.3. Summary

From the preceding analysis, one can draw the following conclusions:

- The identification of the CSP radicals produces a partitioning of the original set of unknowns into two subsets, one consisting of the M CSP radicals and the other of $N - M$ unknowns. The values of the CSP radicals may be found by solving the algebraic relations Eq. (7), whereas the remaining $N - M$ unknowns may be found by solving Eq. (8). For convenience, we will call *minor* species (unknowns) the union of the set of CSP radicals and the set of trace species, and we refer to the remaining species (unknowns) as *major*.

- The unknown y^k is affected by the i-th time scale $\tau_i = 1/|\lambda(i)|$, if $\boldsymbol{\alpha}_i$ has a component along the y^k-axis; i.e., $\boldsymbol{e}^k \cdot \boldsymbol{\alpha}_i \neq 0$; the larger the value of $|\boldsymbol{e}^k \cdot \boldsymbol{\alpha}_i / y_o^k|$, the larger is the effect of the i-th time scale on y^k. The unknown y^k participates in the cancellations occurring in the i-th algebraic relation $f^i \approx 0$, if the y^k-axis has a component along $\boldsymbol{\alpha}_i$; i.e., $\boldsymbol{\beta}^i \cdot \boldsymbol{e}_k \approx 0$; the larger the value of $|\boldsymbol{\beta}^i \cdot \boldsymbol{e}_k\, y_o^k|$, the more significant the participation of the k-th unknown y^k in $f^i \approx 0$. The unknown y^k is a CSP radical when it is both strongly affected by the i-th time scale τ_i and significantly participates in the i-th algebraic relation $f^i \approx 0$; i.e., when both the coefficients $|\boldsymbol{e}^k \cdot \boldsymbol{\alpha}_i / y_o^k|$ and $|\boldsymbol{\beta}^i \cdot \boldsymbol{e}_k y_o^k|$ are non-zero and large. The best conditioning of the underdetermined set of algebraic equations (26) is obtained if one solves them with respect to the M CSP radicals, treating the remaining $N - M$ unknowns as parameters.

- It is possible that $\boldsymbol{\alpha}_i$ has a component along the y^k-axis ($\boldsymbol{e}^k \cdot \boldsymbol{\alpha}_i \neq 0$) but the y^k-axis has no component along $\boldsymbol{\alpha}_i$ ($\boldsymbol{\beta}^i \cdot \boldsymbol{e}_k = 0$); in this case y^k is affected by τ_i but its axis lies on the manifold (so cannot participate in the algebraic relation). The unknown y^k cannot be identified as a CSP radical. It is possible that $\boldsymbol{\alpha}_i$ has no component along the y^k-axis ($\boldsymbol{e}^k \cdot \boldsymbol{\alpha}_i = 0$) but the y^k-axis has a component along $\boldsymbol{\alpha}_i$ ($\boldsymbol{\beta}^i \cdot \boldsymbol{e}_k \neq 0$); in this case y^k is not affected by τ_i but its axis does not lay on the manifold (so participates in the algebraic relation). The unknown $\boldsymbol{y}^k$ cannot be identified as a CSP radical.

- A species is declared a trace species when the criterion (30) holds; a trace species is often

associated with a dormant mode: under this circumstance, both the trace species and the corresponding dormant mode can be safely removed from the governing equations, thus leading to significant computational work savings.

5. Reacting flow problem definition

We consider the interaction of a two dimensional counter-rotating vortex-pair with a premixed methane-air flame. This problem exhibits "turbulence-chemistry interactions" which are very useful for assessing flame behaviour in general turbulent flow. This is due to the significant strain-rate and curvature disturbances to the flame structure, resulting in large changes to radical species concentrations and reaction rates.

The 2D unsteady governing conservation equations are presented in [15]. Here it suffices to say that the assumptions of zero bulk viscosity [21], negligible body forces and low Mach number [22] were employed. In the energy equation, variable transport properties and a constant stagnation pressure are assumed. Soret and Dufour effects, radiant heat transfer, and soot formation are neglected. The model assumes a perfect gas mixture, with individual species molecular weights, specific heats, and enthalpies of formation.

The detailed chemical reaction mechanism GRI-mech1.2 [17] for methane-air chemistry, involving $N_s' = 32$ species, $E = 4$ elements and $N_r = 177$ reversible reactions was employed. Just like the state equation is used to eliminate one of the two unknowns (ρ, T) in favor of leaving T as an integrated unknown with $\rho = \rho(T)$, we use the constraint on the mass fractions $\sum_{i=1,N_s'} Y_i = 1.0$ to eliminate one species from the integrated system. To achieve maximum accuracy, this is chosen to be N_2 (the N_s'-th species), i.e.:

$$Y_{N_2} = 1.0 - \sum_{i=1,N_s'-1} Y_i \tag{31}$$

since N_2 is the species with the largest mass fraction in the mixture. The dimension of the PDE system thus becomes equal to $N = (N_s' - 1) + 1 = N_s$, where $N_s = N_s' - 1$ is the actual number of species considered.

The governing equations are discretized using second-order central differences on a uniform mesh, with cell size $\Delta x = 15.6$ μm. An open rectangular domain is considered, with dimensions 0.4×1.6 cm, and is overlaid by a 256×1024 uniform mesh.

This system exhibits both periodicity and symmetry in the horizontal $\boldsymbol{x}$-direction, depending on the width of the domain being considered. Since we are dealing with only one-half of the vortex-pair, we have symmetry boundary conditions, even though the flow exhibits periodicity at twice this length scale. Outflow boundary conditions are applied in the **y**-direction.

The discrete equations are integrated using an operator-split stiff second-order predictor-corrector projection scheme [15]. Diffusion and convection terms are integrated explicitly with multiple fractional steps, over half-time-step intervals, while the reaction terms are integrated implicitly over a full time-step interval. The explicit half-steps are arranged symmetrically before and after the implicit step in each global step. Stiff integration of reaction terms is performed using DVODE. In the calculations reported here, the Jacobian is evaluated analytically. This problem has been studied in depth in recent literature [16], with extensive comparisons to experimental measurements [23].

6. Results

First, the evolution of the flame and flow field will be illustrated and then the results of the CSP analysis will follow.

6.1. Flow-flame evolution

The evolution of the flow is illustrated in Fig. 1 for a stoichiometric 20% N_2-diluted premixed methane-air flame. The vertical right edge of the domain is the centerline of the vortex-pair under consideration, which is one member of a periodic row of vortex pairs along the x-direction. The initial condition is a superposition of the velocity (u,v) field induced by the periodic row of vortex-pairs, and the temperature, density and mass fraction (T, ρ, Y_i) distributions corresponding to a horizontal premixed flame, with the initial structure in the y-axis direction available from a one-dimensional (1D) flame solution computed with Chemkin [24,25]. The vortex-pair propagates upwards causing transient curvature and strain-rate disturbances to the flame, while the flame propagates downward by burning into the reactants.

The resulting evolution of the flame is illustrated in Fig. 1, using the temperature and heat release rate fields, with the vorticity field superposed on the heat release rate field. During the interaction, the vortex-pair propagates into the flame, leading to significant contortion with large strain-rate and curvature disturbances to the flame. A flame "bubble" is formed, followed by the merging of flame segments behind the vortex-pair and the formation of a burning pocket that continues to propagate downstream until it runs out of fuel.

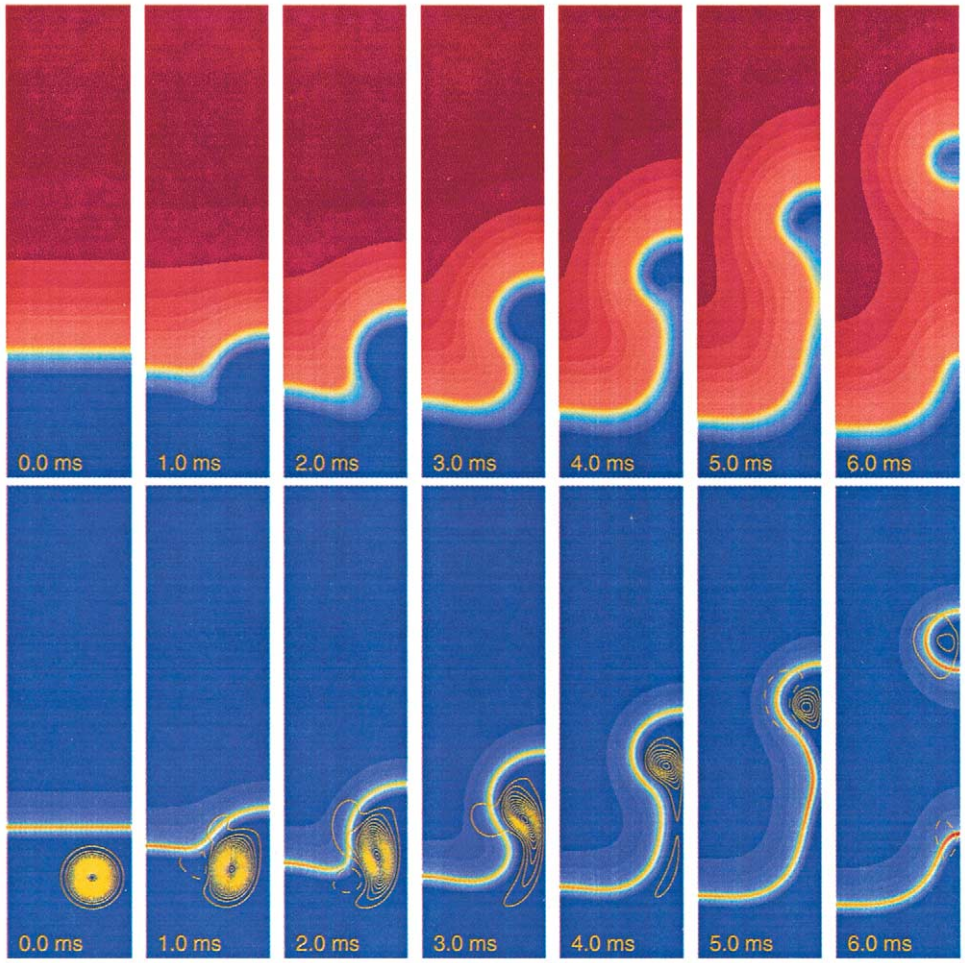

Fig. 1. Flame evolution during the interaction with the vortex-pair. Two frame sequences are shown illustrating flame evolution using the temperature (top) and heat release rate (bottom) fields. The vortex-pair is shown using solid/shaded positive/negative vorticity contours superposed on the heat release rate field.

The flame experiences a large tangential strain-rate disturbance on the vortex-pair centerline, with associated reduction in burning and heat release rate. It also experiences large curvature and normal strain-rate disturbances at the positively curved cusp (convex towards the reactants), which leads to similar reduction in burning and heat release rate in this region [26].

Moreover, the temperature field exhibits significant broadening in the positive cusp region due to the large normal strain-rate, and is found to be entrained to some extent by the convective field behind the vortex. Radicals that are highly unstable in the low temperature reactants region do not exhibit this of course. Similarly, the heat-release rate field, highlighting the primary flame reaction zone, exhibits no broadening in the positive cusp region.

The merging flame segments behind the vortex exhibit an increase in burning and heat release rates as various elements of their reaction zones merge [27]. The heat release rate field exhibits this as expected, as well as a localized increase in the negatively curved flame segments left after reconnection. This increase is the inverse of the observed behaviour at the positively curved cusp, reflecting the inversion of the flame topology curvature and associated focusing/defocusing of species and heat fluxes.

In the following, we use CSP to analyze the above time evolution of various component fields of the flame.

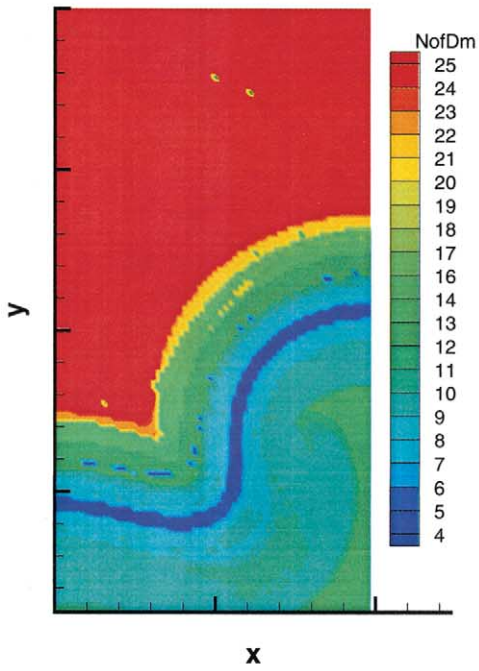

(a) Time 1.8 ms

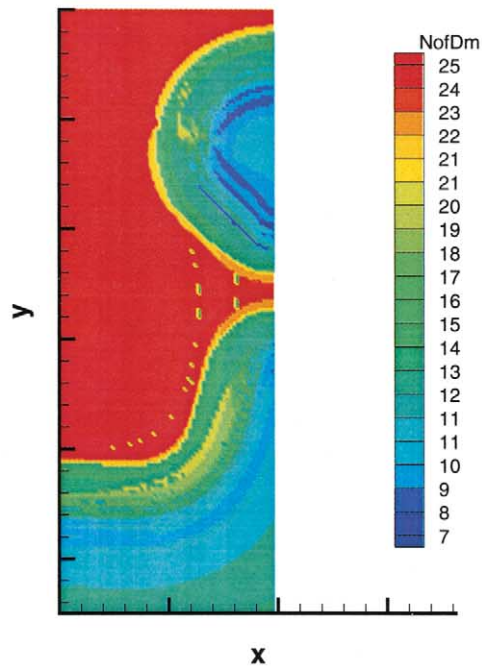

(b) Time 5.0 ms

Fig. 2. Number of exhausted chemical time scales fields at two different times.

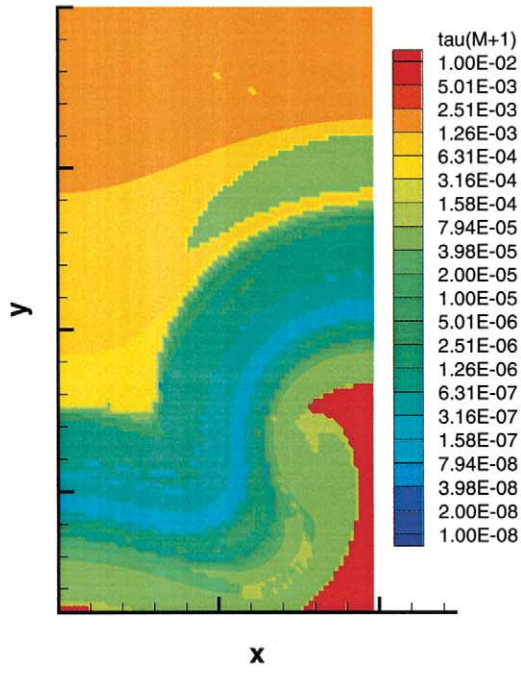

(a) Time 1.8 ms

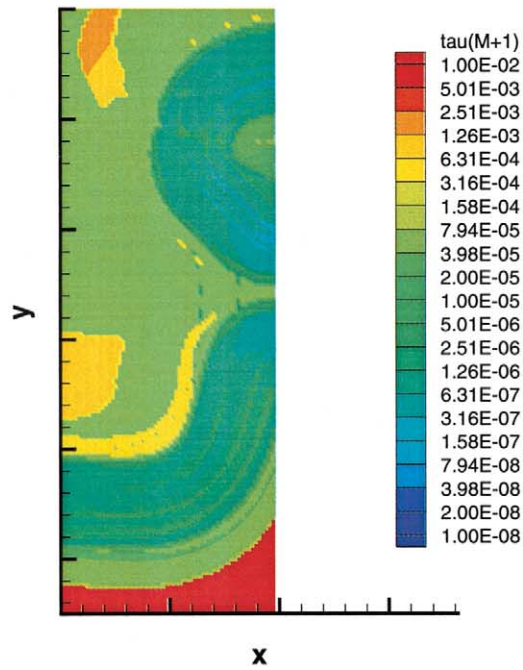

(b) Time 5.0 ms

Fig. 4. Chemical time scale field (τ_{chem}^{M+1} [sec]) at two different times.

6.2. Identification of flow regimes

The first step of the CSP analysis involves finding, at each point in the flow domain, the number of exhausted time scales (according to a user specified accuracy) and the number of exhausted and dormant modes, or else the actual dimensions of the subspace inside which the system space vector moves and of the manifold, at one space location. These decisions are made here using the criteria based on Eq. (10) and Eq. (11) and having set the relative and the absolute errors on the i-th element of the vector $\boldsymbol{y}$ equal to $\epsilon^i_{rel} = 10^{-3}$ and $\epsilon^i_{abs} = 10^{-13}$, respectively.

The analysis is carried out over the whole flowfield. The variation of M (the number of exhausted chemical time scales) in the flow domain is shown in Figs. 2(a) and 2(b), for times 1.8 and 5.0 ms, respectively. The color map in each figure indicates the number of exhausted chemical time scales, as indicated. At the top of the domain, the red region corresponds to the largest number of exhausted time scales (26) with 8 exhausted modes and 18 dormant. Since the number of unknowns is $N = 32$, the actual dimension of the manifold in the product region is $N - M = 32 - 26 = 6$, since all dormant modes are found to be fast. This means that, there, the flow state variables vary only because of the action of 6 modes, 4 (E = 4) of which are chemistry free and the remaining 2 involve both chemistry and transport. These modes evolve at the (slow) chemical time scale of the $M + 1 = 27$-th eigenvalue, which is also the driving time scale here.

Inspection of the flame topology in Fig. 1 indicates that this region corresponds to the product region behind the premixed flame. The CSP results confirm the qualitative expectation that the hot products approach equilibrium as they move beyond the primary flame. Besides this confirmation, however, the results provide a clear quantification of the equilibrium manifold dimension and of its topological variations with distance from the flame.

Moving down towards the flame sheet, the manifold dimension gradually increases until, as we approach the primary reaction zone, we observe a fast transition to a very narrow region where just a few modes are exhausted ($M = 4 - 8$), which, in blue, reveals the outline of the reaction zone curvature and extension in the domain according to the heat release and temperature fields shown in Fig. 1. Here again, we have a confirmation of the qualitative expectation that almost all time scales become active in the primary reaction zone. However, we also have the additional quantification that four modes have indeed become exhausted in this region, at least per the specified relative and absolute error tolerances.

We note that high accuracy of the computational results is a prerequisite for finding exhausted modes in the flame. Very small errors in the mass fraction and temperature fields can cause the flame solution to be slightly off the manifold, by such an extent that the amplitudes of several of the fastest modes are not exhausted any more. This will reduce the number of exhausted chemical time scales, and increase the manifold dimension, inside the flame. High time integration accuracy can be ensured by using sufficiently small time steps and/or high order integrators. In the context of second-order Strang splitting higher accuracy can be achieved for a given time step if the stiff operator is applied last in the time step [28].

Flame radicals are found to be essentially nonexistent, and reaction rates to be zero as one leaves the primary reaction zone and approaches the frozen flow region of cold reactants. The flow evolution here is driven primarily by convection and diffusion, and the only species found here, other than the reactants, are just a few stable species transported away from the flame front into the cold reactants region. As a consequence, the very small reaction rates make the modes associated to the fastest chemical time scales dormant ($M = 13 - 14$, see Figs. 2(a) and 2(b)). Therefore, no manifold develops here. Nevertheless, the trajectory loses M degrees of freedom, one for each dormant mode. The first non-vanishing mode amplitude, which sets the local driving time scale, develops along the direction the slower chemical time scales act, because the projection of the transport terms along the corresponding direction becomes non negligible, that is: $h^{M+1} = \boldsymbol{b}^{M+1} \cdot \boldsymbol{L} \neq 0$. As a result, we observe generally small variations in the number of exhausted chemical time scales in this region, reflecting active convective and diffusive processes. Thus, for example, we see in Fig. 2(a) contours of slight variation in the number of exhausted chemical time scales that reveal the convective entrainement by the vortex, the tangentially stretched, hence normally compressed, region ahead of the vortex (cf. Fig. 1), and the tangentially compressed, normally stretched, positively curved cusped region.

The number of exhausted chemical time scales at $t = 1.8$ ms is plotted along the vortex-pair centerline (cf. Fig. 1) in Fig. 3(a) to provide the reader with a clearer delineation of its variation. The plot shows the variation of temperature along the centerline, to allow the identification of the primary flame reaction zone. The variation of M is superposed. The results indicate the high value of $M = 26$ in the product region, the presence of just a few exhausted chemical time scales in the narrow reaction zone region, and the uniformly intermediate number ($M = 13 - 14$) of exhausted chemical time scales due to the emergence of dormant modes in the reactants.

Note that as we proceed from the cold reactants

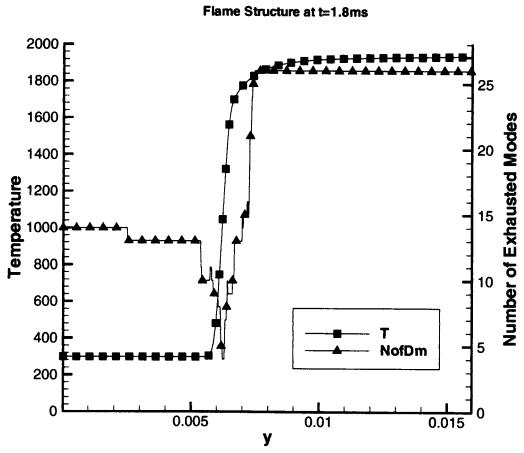

(a) Time 1.8 ms

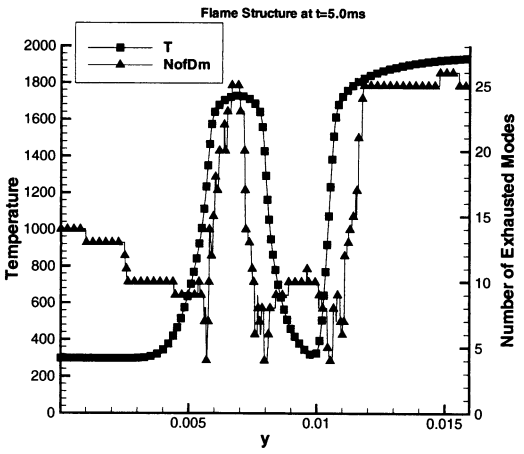

(b) Time 5.0 ms

Fig. 3. Number of exhausted chemical time scales along the vortex-pair centerline at two different times; triangles denote number of exhausted chemical time scales, squares denote temperature [K].

into the preheat zone, M decreases from the value of 14 in the frozen flow region down to 4-6 in the flame due to the onset of chemical activity prompted by diffusion of species and heat ahead of the primary flame zone.

Figure 2(b) shows the variation of M at $t = 5.0$ ms throughout the computational domain, while Fig. 3(b) shows the evolution of M and T along the vortex centerline. At this time, two flame regions have merged along the vortex-pair centerline and have isolated a pocket of reactants which keeps burning independent of the main flame front.

The temperature field in Fig. 3(b) reveals a broad region of higher temperature with a peak at around 1700K between the pocket of reactants and the main flame front. The highest temperature is found downstream of the pocket of reactants and reaches about 1900K. The temperature in the reactants is still at about 300K, both ahead of the main flame front and inside the pocket of reactants. The associated chemical activity leads to the observed variation of M in this region, with a minimum number of exhausted chemical time scales in the high-heat release regions where reaction rates are fast, radical species concentrations are high and the temperature gradient steep. The number of exhausted chemical time scales rises to 26 where hot products have reached a near-equilibrium condition.

In the frozen flow region, the number of exhausted chemical time scales attains again the 13-14 value.

Therefore, as Fig. 3(b) shows, along the centerline there exists three regions of minimal number of exhausted chemical time scales, corresponding to the regions of high heat release in the three primary flames seen in Fig. 1.

To conclude this discussion, it is worth emphasizing that the manifold dimension is not uniform neither spatially nor temporally during the transient vortex/flame interaction, as clearly demonstrated by the large spatial and temporal variations occurring in the number of exhausted chemical time scales. From another point of view, the choice of using one single manifold dimension, to be enforced throughout the whole flowfield and at all times, is bound to be affected by errors which will likely be proportional to the difference between the assumed manifold dimension and the actual dimension found by adopting the criterion (10).

6.3. Time scales

The chemical time scale field, given by $\tau_{chem}^{M+1}(\mathbf{x}, t)$, is shown in Figs. 4(a) and (b) at times 1.8 and 5 ms, respectively. In both figures, the results outline clearly that the fastest active time scales arise in a narrow strip corresponding to the primary flame reaction zone as contorted and stretched by the vortex-pair. This is in agreement with the expectation that the fastest rates of change in species concentrations occur in the reaction zone.

At time 1.8 ms and in the flame zone, convection proceeds at a slower pace than diffusion and both the diffusion and convective time scales, as estimated by the relations [17], are slower than the chemical time scale (Fig. 5(a)). Therefore, the driving time scale, $\tau_{driving}$, as defined according to the relation [18], originates from chemical reactions.

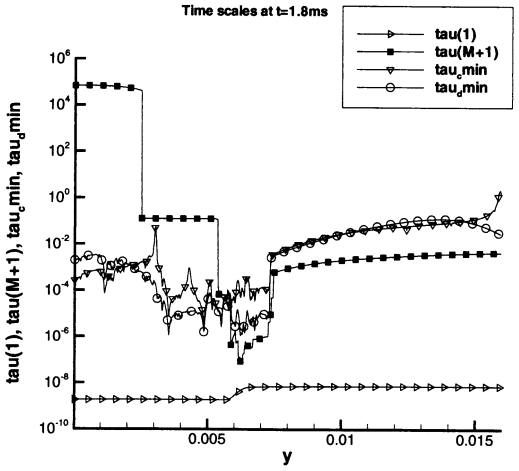

(a) Time 1.8 ms

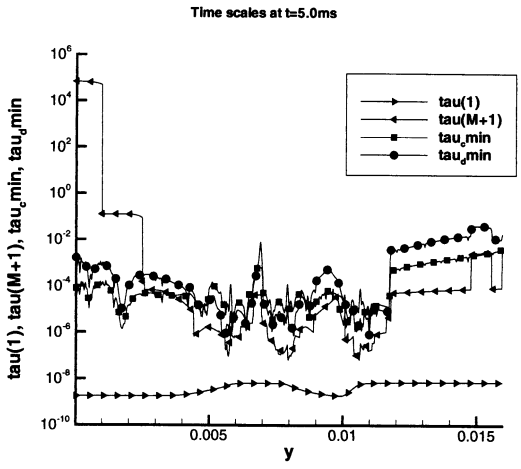

(b) Time 5.0 ms

Fig. 5. Convective, diffusive and chemical time scales (τ^1_{chem} and τ^{M+1}_{chem} [sec]), at two different times along the vortex-pair centerline.

Proceeding towards the products, slower rates of change are indicated by the increasing values of the driving time scales, which approach $\tau^{M+1}_{chem} = 1$ ms towards the domain exit. In accordance with the observations displayed in Figs. 2(a) and 2(b), more and more fast chemical time scales become exhausted as we move away from the primary flame towards the products. Both the diffusive and convective time scales, as found inside the flame, are slower than the chemical scale, which, as shown in Figs. 5(a) and 5(b), is still the driving time scale.

Slow time scales characterize the chemical processes only in the cold reactants zone, due to the absence of any chemical activity at the prevailing low temperature. Therefore, it is proper to define this flow regime as frozen. As shown in Figs. 4(a) and 4(b) throughout the region and in Figs. 5(a) and 5(b), along the vortex-pair centerline, τ^{M+1}_{chem} is quite slow, reaching very large values. In contrast, Fig. 5(a) shows that convection and diffusion are much faster than chemistry, the diffusion being the fastest. As a result, the driving time scale is set by diffusion.

Figure 5(a) also shows the variation of the fastest time scale τ^1_{chem}, which is smallest in the reactants at 1 ns and slightly larger in the products at 10 *ns*. The largest separation between the locally driving and the fastest chemical time scale, i.e., the largest ratio $\tau_{driving}/\tau^1_{chem}$, is found in the reactants region, followed by that in the products, with the smallest separation in the flame. Consequently, the stiffness of the time-integration problem is expected to be most severe in the reactants, milder in the products, and essentially absent in the primary flame.

We note that previous experience [29,30] indicates that stiff integration of this system using either semi-implicit or operator-split time integration with the ODE integration package DVODE [31] used for the chemical source terms highlighted the large time integration effort, due to increased number of function and Jacobian evaluations per time step, in the flame region, with less effort in the products, and least in the reactants. The present results indicate clearly that this circumstance is not due to stiffness, but rather due to the smaller internal time steps required in the stiff integrator for maintaining time-accuracy in the products and primary flame regions, where fast rates of change of species concentrations are exhibited. Despite the large stiffness in the reactants, with $\tau_{driving}/\tau^1_{chem} \sim 10^6$, a stable implicit time integration requires minimal numbers of function and Jacobian evaluations as the actual rates of change are negligible.

We also note that the spatial variations in $\tau_{driving}$ shown in Fig. 5(b) are due to the merging flames on the centerline, and mirror the corresponding variation in M in Fig. 3(b). Further, we note that τ^1_{chem} is increasing within the zone of flame merging and tends to attain the same value found in the product region, since there the reactants have been converted into products.

6.4. Classification of unknowns (species)

After the identification of the regions characterized by different flow regimes and manifold dimen-

Table 1
Time scale estimates (in seconds) for the 4 exhausted modes at time 1.8 ms, at a point inside the flame region at the vortex-pair centerline ($y = 6.26$ mm)

Mode No.	τ_{chem}	τ_{conv}	τ_{diff}
1	2.48E−06	6.98E−01	8.60E−03
2	8.80E−06	1.27E−01	9.86E−04
3	1.30E−05	1.96E+00	6.72E−02
4	1.41E−05	9.21E−01	5.04E−01

Note that the modes are ordered according to the value of the corresponding chemical time scale.

sions, and after having found proper estimates of the relevant flow time scales, we can now proceed in the classification of the unknowns according to the analysis carried out in section 4. We analyze the flow inside the flame at $y = 6.26$ mm and time 1.8 ms, and we find that the first 4 modes have become exhausted (see Table 1). The timescale estimates computed according to Eq. (17) allow us to conclude that, at this location, the driving scale is set by chemistry ($O(2 - 14)$ μs), whereas diffusion proceeds at a slower pace ($O(1 - 500)$ ms) and convection is even slower ($O(0.1 - 2)$ s).

At this stage we are able to find the answers to the questions posed in section 4.1 as applied in the present context. First, we have to compute the CSP pointers $\alpha_i^k \beta_k^i$ and the coefficients $|(\boldsymbol{e}^k \cdot \boldsymbol{\alpha}_i)/y_o^k|$ and $|(\boldsymbol{\beta}^i \cdot \boldsymbol{e}_k) y_o^k|$. These have been sorted in descending order and collected in the three columns of Table 2 respectively, for the 4 exhausted modes included in Table 1. Inspection of the first column reveals that for each mode only one species has a large CSP pointer, that is a large value of $\alpha_i^k \beta_k^i$. This allows us to identify the species $CH_2(S)$, CH, C and C_2H as the CSP radicals and associate them with the 4 exhausted modes.

At this point, for simplicity, let us focus our attention on only one mode, say the second mode. We can read from the second column of Table 2 that the species most affected by the (fast) chemical time scale of the second mode ($\tau_2 = 8.80$ μs) are C, CH followed at a distance by HCO, CH_2, O, whereas, from the third column of Table 2, we find that the species contributing most to the algebraic equation $h^2 \approx 0$ are Temperature, CH_2, CH, H, and O_2. The absence of O_2, H and T from the second column implies that they are not affected by the fast time scale, hence their time rates of change is set by slow

Table 2
Classification of unknowns at time 1.8 ms, at a point inside the flame region at the vortex-pair centerline ($y = 6.26$ mm)

Name	$\alpha_i^k \beta_k^i$	Name	$\lvert(\boldsymbol{e}^k \cdot \boldsymbol{\alpha}_i)/y_o^k\rvert$	Name	$\lvert(\boldsymbol{\beta}^i \cdot \boldsymbol{e}_k) y_{ok}\rvert$
Mode No. 1					
CH2(S)	9.97E − 01	CH2(S)	4.27E + 06	CH2(S)	2.33E − 07
CH2	3.02E − 03	CH2	1.45E + 05	CH3	2.12E − 07
OH	1.16E − 04	CH	2.22E + 04	OH	2.05E − 07
CH3	1.28E − 05	C	4.97E + 03	T	9.34E − 08
H	1.27E − 06	CH2OH	1.79E + 03	H2O	5.13E − 08
Mode No. 2					
CH	1.00E + 00	C	1.21E + 08	T	2.27E − 08
CH2	4.72E − 05	CH	6.03E + 07	CH2	1.80E − 08
H	3.43E − 06	HCO	1.18E + 04	CH	1.66E − 08
C	4.11E − 07	CH2	2.62E + 03	H	1.61E − 08
CH2(S)	1.86E − 07	O	1.46E + 03	O2	5.87E − 09
Mode No. 3					
C	1.00E + 00	C	8.70E + 09	T	4.52E − 10
CH	4.12E − 07	C2H	4.14E + 04	H	4.45E − 10
O	1.42E − 09	CH	1.79E + 03	CH2	3.94E − 10
C2H	1.37E − 09	O	1.32E + 03	CH	2.31E − 10
CH2	4.20E − 10	CH2OH	3.47E + 01	O2	2.07E − 10
Mode No. 4					
C2H	1.00E + 00	C2H	7.04E + 08	T	9.77E − 09
C2H2	4.25E − 07	C	1.75E + 05	C2H	1.42E − 09
OH	3.37E − 07	CH	1.43E + 04	OH	1.41E − 09
T	2.60E − 09	HCO	1.02E + 04	C2H2	1.41E − 09
HCO	1.64E − 09	C2H2	3.01E + 02	O2	8.89E − 10

The number of exhausted chemical time scales is 4. Only the first 5 rows are shown for each mode, corresponding to the 5 largest values of the corresponding index.

Table 3
Elementary reactions most contributing to the algebraic relation $h^2 \approx 0$

fw	$CH+O_2 <=> O+HCO$
fw	$CH+CH_4 <=> H+C_2H_4$
fw	$OH+CH_3 <=> CH_2(S)+H2O$
fw	$CH+H_2O <=> H+CH_2O$
fw	$CH+H_2 <=> H+CH_2$
fw	$CH_2(S)+N_2 <=> CH_2+N_2$
bw	$CH+H_2 <=> H+CH_2$
fw	$CH_2+O_2 <=> OH+HCO$

processes. On the other hand, their presence in the third column implies that they participate in the algebraic relation $h^2 \approx 0$. Note that neither C nor temperature which are ranked first in columns two and three respectively, are chosen as CSP radical for this mode. Indeed, species CH becomes the CSP radical, since it has by far the largest CSP pointer ($\alpha_2^{CH}\beta_{CH}^2$) (in the first column) and is a major participant in both the second and third columns.

These findings are confirmed by the set of elementary reactions, shown in Table 3, which establish the relation between the CSP radical CH and the major unknowns O_2, H, and T. These reactions were identified as those contributing the most to the cancellations occurring in the relation $h^2 \approx 0$. Other major species intervene in this set of elementary reactions, such as H_2O, OH, CH_4, O, and H_2, which are not ranked among the first 5 listed in Table 2 because they just happen to fall below the threshold used to select the top 5 species.

Since the second mode is exhausted, i.e., the trajectory satisfies the $h^2 \approx 0$ constraint, these findings indicate that the time rate of change of CH will not be related to τ_2, but will depend mostly on the slower rates of change of O_2, H, T as well as H_2O, OH, CH_4, O, and H_2. On the other hand, CH will react according to τ_2 if any perturbations displace the trajectory off the manifold, so that h^2 becomes non-zero. This also implies that h^2 will vanish again, as CH reapproaches the manifold, within a time span of the order of τ_2.

Note also that temperature is ranked first, not only among the unknowns contributing to the equation $h^2 \approx 0$, but also for modes 3 and 4: this reflects the circumstance that the heat release due to chemistry (which mostly affects temperature) is the main slow process driving all the fast and slow kinetics.

We can now expand the analysis by identifying the CSP radicals and the species in trace status, as we move along the vortex-pair centerline at two different times. The results, shown in Fig. 6, were collected with a threshold for the identification of the trace species in Eq. (30) set equal to 10^{-12} (mass fraction).

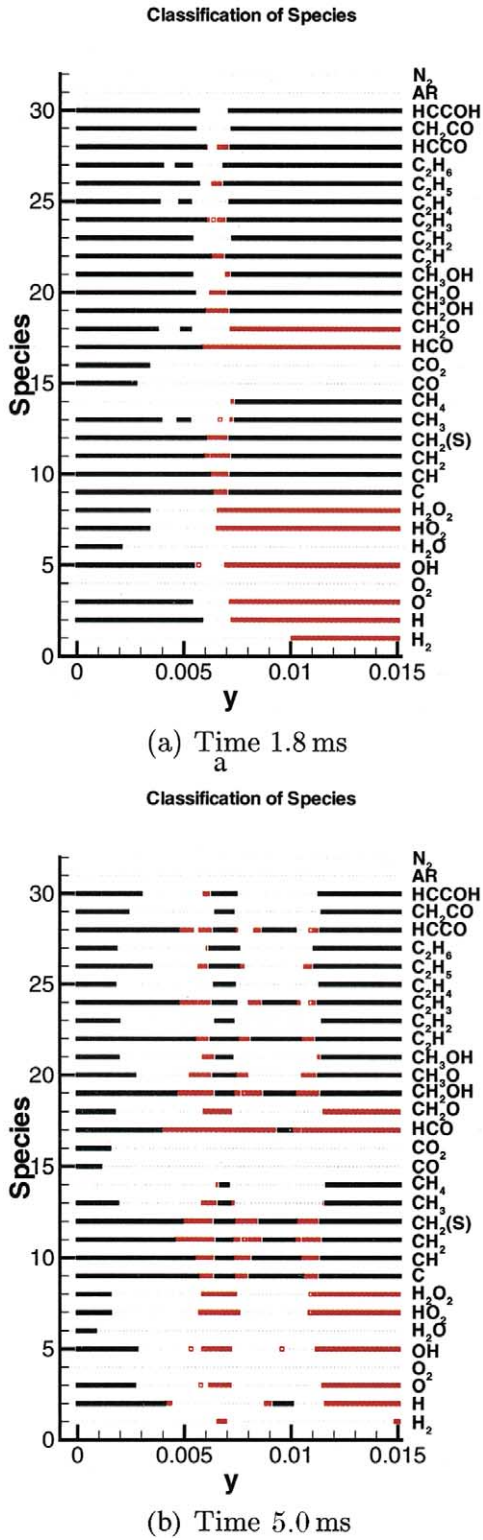

Fig. 6. Black and red markers denote "trace" species and CSP radicals respectively, along with the vortex-pair centerline at two different times.

In the figure, black and red markers indicate trace species and CSP radicals, respectively.

At time 1.8 ms, the region in the vicinity of $y = 6.6$ mm in Fig. 6(a) corresponds to the flame zone, where fewer exhausted modes are found. Ahead of the flame ($y < 6.6$ mm), there exists 27 trace species. The remaining 5 major species, including the fuel CH_4, the air constituents N_2 (per Eq. (31)), O_2, and Ar and molecular hydrogen H_2, as well as temperature, are convected and diffused from the flame cusp towards the vortex-pair centerline.

The 27 trace species can be associated with the 14-15 fast dormant modes and the remaining slow dormant modes in this region: they could be neglected without affecting the solution accuracy. These dormant modes are characteristic of the frozen flow regime ahead of the flame front.

Figure 6(a) shows that CSP radicals (marked in red) are present both inside the flame and downstream of it.

In the equilibrium zone located downstream of the flame, there are:

- 8 CSP radical species: H_2, H, O, OH, HO_2, H_2O_2, HCO and CH_2O, whose dynamics are controlled by the fast time scales when the trajectory is off the manifold, and whose values are determined by only 8 exhausted modes (found among the 26 exhausted chemical time scales) when the trajectory is on the manifold;
- 6 major unknowns, that is the 5 species: O_2, H_2O, CO, CO_2, Ar, and temperature whose dynamics, evolving at the chemical time scale τ_{chem}^{27}, are determined by only 32-26 = 6 active modes (note that N_2 is also enlisted as a major species according to Eq. (31));
- the remaining 32-8-6 = 18 species are in trace status and they can be safely eliminated from the list of the actual unknowns together with the dormant modes pointing to them.

Inside the flame, there are from 4 to 10 exhausted modes, that is at most 4 to 10 CSP radicals. Among these we can list: C, CH, CH_2, CH_2(S), HCO, CH_2OH, CH_3O, C_2H, C_2H_5, and HCCO. However, the discrimination of CSP radicals inside the flame is solely made on the basis of the user defined accuracy (ε_{rel} and ε_{abs}) and it is not an intrinsic property of the flow. This occurs because the spectrum of the chemical time scales inside the flame is dense with no major time scale separation occuring there. As a consequence, the manifold dimension, i.e., the splitting of the source term into fast and slow contributions, is also based on an accuracy requirement only.

Note that there are 7 species that are minor (either CSP radicals or trace species) throughout most of the flow domain. These are: C, CH, CH_2, CH_2(S), HCO, CH_2OH, and C_2H. The conservation equations corresponding to these 7 species can therefore be eliminated in a reduced kinetic mechanism which will include as major species only 25 of the original 32 species. The remaining minor species are found by solving the algebraic relations that define the manifold.

Comparing Fig. 6(b) with Fig. 6(a) clearly shows that the species switch among the possible status of trace, CSP radical and major species both in time and space so as to adjust to the unsteady flow conditions. Fig. 6(b) shows that, at time 5.0 ms, as many as 15 species are CSP radicals in the region between the main flame front and the pocket of isolated reactants, whereas only 7 CSP radicals are found downstream of the pocket of reactants.

Where the flames have merged at the vortex-pair centerline, there are among the hot products 7 CSP radicals (H_2, O, OH, HO_2, H_2O_2, HCO, and CH_2O) and 7 major species (H, O_2, H_2O, CO, CO_2, Ar, and N_2) and temperature.

At time 5.0 ms, 7 species are minor over most of the flow domain, and they are the same as those found at time 1.8 ms. This supports the hope of finding a reduced kinetic mechanism accurate enough over an extended range of spatial and time locations. This reduced or simplified mechanism is found with specific error thresholds, and therefore it has a known error estimate [4]. This is an important feature of the CSP approach in as much as it provides us with a mechanism simplification strategy with a quantification of the errors relative to the full mechanism.

7. Conclusions

In this work, we extended the CSP theory to the realm of PDEs, including convection and diffusion terms. We presented the canonical CSP formulation of the PDE problem involving governing species and energy equations. We also presented a new formulation for the convective and diffusive time scales acting along the fast chemical directions which identify the manifold. We also revised and elaborated the concept of the CSP radical. In particular, we examined the quantities contributing to the choice of CSP radicals at a point in the flame. We highlighted how a species must be both affected by the fast time scales, and participate in the algebraic relationships that define the manifold in order to qualify as a CSP radical candidate. This information provides a clear physical meaning behind the observation that a species is pointed to by the CSP pointer, as a CSP radical.

We then used these extended CSP concepts to analyze a relevant multidimensional, time evolving, reacting flow computed with detailed methane-air kinetics. The outcome of this analysis revealed the spatial distribution of the number of exhausted chemical time scales, reflecting ongoing physical processes in different regions of the flow. This information was found to be both consistent with physical expectations and to provide useful quantification of the size of the equilibrium manifolds in different regions of the evolving flow-field. The results highlight three major regions in this premixed flow,

- A frozen chemistry region in the cold reactants where 13-14 modes are dormant.
- A near-equilibrium region in the products where 18 dormant modes and 8 exhausted modes are evident.
- The primary reaction zone where most modes are active, and only 4-8 modes are exhausted.

The distribution of exhausted/dormant modes was found to faithfully describe the evolution and contortion of the flame, as well as the process of pocket formation and the effect of the vortex in the cold reactants.

We established that no low dimensional manifold develops valid throughout the computational domain. In addition, our results show clearly that deriving a manifold from one spatio-temporal location and using it globally can be a source of error. Requiring reasonably high accuracy, adequate model reduction must use a manifold of sufficiently high dimensionality such that it is valid throughout the domain and during the whole transient time evolution of the flow. Of course, lowering the accuracy requirements will result in lowering the dimensionality of such a global manifold, producing a much more simple reduced model.

The analysis also highlighted the need for high accuracy in the computed numerical solution in order to ensure accurate source terms, particularly in the flame region where large source terms are prevalent. More specifically, we found that splitting errors resulting from operator-split time integration at large time steps can lead to a slight deviation of the solution from the fast manifold. While this is barely noticeable in the species concentration profiles, the resulting rates of the fast reactions were significantly affected, with consequences to the CSP analysis in the primary reaction zone. Namely, *all* time scales were found active in this zone. Adequate relaxation of the solution with smaller time steps was sufficient to eliminate these artifacts, giving some (4-8) exhausted modes in the flame with a 10^{-3} relative error tolerance.

We also reported the variation of time scales in the evolving flame-flow interaction. We identified chemical, diffusive, and convective time scales, and examined their relative magnitudes in each of the above flow regions. This analysis provided the following conclusions,

- The fastest time scale was always chemical, and was found to be on the order of 1-10 ns.
- The driving chemical time scale was found to be exceedingly large in the frozen chemistry region in the cold reactants. On the other hand, it is on the order of 0.1-1 μs in the flame, and 1 ms in the products.
- The driving chemical time scale (the fastest of the non-exhausted chemical time scales) was found to be faster than the fastest transport time scales both in the flame and the products regions.
- Diffusion was found to generally provide the fastest time scale, on the order of 1 ms, in the reactants region.

Chemical stiffness, defined as the ratio between the driving and fastest chemical time scales, was found to be the highest in the reactants, and least in the flame. Despite the low stiffness in the flame region, the fast rate of change in time leads to the need for small time steps in this region in the context of time integration.

We also investigated the spatial distributions of major and minor species at different points in time. This classification of species is a prerequisite for simplification/reduction of the chemical mechanism with controlled known errors. Species were classified either as: 1) "minor", which includes both "CSP radicals" and "trace" species, and whose concentrations could be found from algebraic constraints; or 2) "major" which includes the remaining species whose concentrations are integrated in time. Looking at the flow-flame interaction at two time instances, we identified major and minor species at different locations in space-time. Based on this analysis, and on specified error tolerances, we find the seven species: C, CH, CH_2, CH_2(S), HCO, CH_2OH, and C_2H, to be minor throughout the domain, and in time. Thus, in this flowfield, the governing equations for these species can be safely exchanged for the appropriate algebraic expressions, within the specified error tolerances for the specification of the manifold and trace species. We recall that no significant separation of time scales is found in the primary flame reaction zone, hence the identification of a manifold and CSP radicals there is strictly a function of the specified error tolerances.

In future work we will pursue parametric studies

of this flame-vortex interaction with vortex-pairs of varying sizes and strengths, in order to examine the dependence of the CSP-reduced mechanism on variations in the strain-rate and curvature disturbances to the flame, and the corresponding spatiotemporal scales prevalent the flow field. This study is necessary to establish the robustness of the above reduced mechanism to different flow conditions.

As a general final comment, we would say that this work has shown how the CSP analysis results, including the identification of exhausted modes, equilibrium manifolds, time scales, and major/minor species, enable automatic model reduction at any location in a PDE reacting flow model. With appropriate control of computational costs, this analysis has potential application in future adaptive chemistry models for computations of time evolving reacting flow using optimal locally adaptive kinetic mechanisms.

Acknowledgments

This work was supported by the Department of Energy, Office of Basic Energy Sciences, SciDAC Computational Chemistry Program, the Italian Space Agency (ASI) and the Italian Ministry of Education, University and Research (MIUR). The work has profited from the suggestions, criticisms and review of Prof. Harvey Lam, of Princeton University, to whom we express our gratitude. We also acknowledge many fruitful discussions with Prof. Omar Knio, of The Johns Hopkins University.

References

[1] S. Lam, D. Goussis, Twenty-Second Symposium (International) on Combustion, The Combustion Institute, Pittsburgh (1988) p. 931.
[2] U. Maas, S. Pope, Twenty-Fourth Symposium (International) on Combustion, The Combustion Institute (1992) pp. 103–112.
[3] F. Williams, Combustion Theory, 2nd Edition, Addison-Wesley, New York, 1985.
[4] D. Goussis, J. Comput. Physics 128 (1996) 261.
[5] E. Hesstvedt, O. Hov, I. Isaksen, Int. J. Chem. Kinetics 10 (1978) 971–994.
[6] S. Lam, Combust. Sci. Technol. 89 (1993) 375–404.
[7] S. Lam, D. Goussis, Int. J. Chem. Kinetics 26 (1994) 461–486.
[8] M. Hadjinicolaou, D. Goussis, SIAM J. Sci. Comp. 20 (1999) 781.
[9] A. Massias, D. Diamantis, E. Mastorakos, D. Goussis, Combust. Flame 117 (1999) 685–708.
[10] N. Peters, In: R. Glowinski, B. Larrouturou, R. Teman (Eds.), Numerical Simulation of Combustion Phenomena, no. 241, Springer-Verlag, New York, 1985, lecture Notes in Physics.
[11] A. Tomlin, T. Turanyi, M. Pilling, Oxidation Kinetics and Autoignition of Hydrocarbons, Elsevier, New York (1997) pp. 293–437.
[12] V.P. Vajda S., T.T., Int. J. Chem. Kinetics 12 (1985) 17–55.
[13] N.D. Lovas T., M.F. Proc. Combust. Inst. 28 (2000) 1809–1817.
[14] J.Y. Lu T.F., L. C.K., Combust. Flame 126 (2001) 1445–1455.
[15] H. Najm, O. Knio, P. Paul, P. Wyckoff, Combust. Theory and Modelling 3 (4) (1999) 709–726.
[16] O. Knio, H. Najm, Proc. Combust. Inst. 28 (2000) 1851–1857.
[17] M. Frenklach, H. Wang, M. Goldenberg, G. Smith, D. Golden, C. Bowman, R. Hanson, W. Gardiner, V. Lissianski, GRImech—an Optimized Detailed Chemical Reaction Mechanism for Methane Combustion, Top. Rep. GRI-95/0058, GRI (Nov. 1995).
[18] S. Lam, D. Goussis, Proceedings of the Central States Section Meeting, The Combustion Institute, Dearborn, Michigan, 1989.
[19] D. Goussis, S. Lam, Twenty Fourth Symposium (International) on Combustion, The Combustion Institute, Pittsburgh (1992) 113–120.
[20] M. Valorani, D. Goussis, J. Comput. Phys. 168 (2001) 1–36.
[21] H. Schlichting, Boundary-Layer Theory, 7th Edition, McGraw-Hill, New York, 1979.
[22] A. Majda, J. Sethian, Comb. Sci. Technol. 42 (1985) 185–205.
[23] H. Najm, P. Paul, A. McIlroy, O. Knio, Combust. Flame 125 (1-2) (2001) 879–892.
[24] R. Kee, F. Rupley, J. Miller, Chemkin-II: A Fortran Chemical Kinetics Package for the Analysis of Gas Phase Chemical Kinetics, Sandia Report SAND89-8009B, Sandia National Labs., Livermore, CA (August 1993).
[25] R. Kee, J. Grcar, M. Smooke, J. Miller, A Fortran Program for Modeling Steady Laminar One-Dimensional Premixed Flames, Sandia Report SAND85-8240, Sandia National Labs., Livermore, CA (September 1993).
[26] H. Najm, P. Wyckoff, Combust. Flame 110 (1-2) (1997) 92–112.
[27] J. Chen, T. Echekki, W. Kollmann, Combust. Flame 116 (1999) 15–48.
[28] B. Sportisse, An analysis of operator splitting techniques in the stiff case, J. Comp. Phys. 161 (2000) 140–168.
[29] H. Najm, P. Wyckoff, O. Knio, J. Comp. Phys. 143 (2) (1998) 381–402.
[30] O. Knio, H. Najm, P. Wyckoff, J. Comp. Phys. 154 (1999) 428–467.
[31] P. Brown, G. Byrne, A. Hindmarsh, SIAM J. Sci. Stat. Comput. 10 (1989) 1038–1051.